energies

MDPI

Article

Artificial Intelligence for the Control of Speed of the Bearing Motor with Winding Split Using DSP

José Raimundo Dantas Neto [1,†], José Soares Batista Lopes [2,†], Diego Antonio De Moura Fonsêca [1,†], Antonio Ronaldo Gomes Garcia [3,†], Jossana Maria de Souza Ferreira [4,†], Elmer Rolando Llanos Villarreal [3,*,†] and Andrés Ortiz Salazar [1,†]

[1] Department of Computer Engineering and Automation, Federal University of Rio Grande do Norte (DCA-UFRN), Natal 59072-970, Brazil; jose.raimundo@ifce.edu.br (J.R.D.N.); diegomoura@dca.ufrn.br (D.A.D.M.F.); andres@dca.ufrn.br (A.O.S.)
[2] Federal Institute of Education, Science and Technology of Rio Grande do Norte (IFRN), Natal 59015-300, Brazil; jose.soares@ifrn.edu.br
[3] Department of Natural Sciences, Mathematics, and Statistics, Federal Rural University of Semi-Arid (DCME-UFERSA), Mossoró 59625-900, Brazil; ronaldogarcia@ufersa.edu.br
[4] School of Science & Technology, Federal University of Rio Grande do Norte (ECT-UFRN), Natal 59072-970, Brazil; jossana.ferreira@ufrn.br
* Correspondence: elmerllanos@ufersa.edu.br
† These authors contributed equally to this work.

Abstract: This article describes the study and digital implementation of a system onboard a TMS 3208F28335 ® DSP for vector control of the bearing motor speed with four poles split winding with 250 W of power. Smart techniques: ANFIS and Neural Networks were investigated and computationally implemented to evaluate the bearing motor performance under the following conditions: operating as an estimator of uncertain parameters and as a speed controller. Therefore, the MATLAB program and its toolbox were used for the simulations and the parameter adjustments involving the structure ANFIS (Adaptive-Network-Based Fuzzy Inference System) and simulations with the Neural Network. The simulated results showed a good performance for the two techniques applied differently: the estimator and a speed controller using both a model of the induction motor operating as a bearing motor. The experimental part for velocity vector control uses three control loops: current, radial position, and speed, where the configurations of the peripherals, that is, the interfaces or drivers for driving the bearing motor.

Keywords: bearingless; DSP; induction motor; radial position control

check for updates

Citation: Dantas Neto, J.R.; Lopes, J.S.B.; Fonseca, D.A.D.M.; Garcia, A.R.G.; Ferreira, J.M.d.S.; Villarreal, E.R.L.; Salazar, A.O. Artificial Intelligence for the Control of Speed of the Bearing Motor with Winding Split Using DSP. *Energies* **2024**, *17*, 1029. https://doi.org/10.3390/en17051029

Academic Editors: Zbigniew Hanzelka, Daniel Morinigo-Sotelo, Grzegorz Sieklucki and Tomasz Drabek

Received: 20 December 2023
Revised: 16 January 2024
Accepted: 12 February 2024
Published: 22 February 2024

Copyright: © 2024 by the authors. Licensee MDPI, Basel, Switzerland. This article is an open access article distributed under the terms and conditions of the Creative Commons Attribution (CC BY) license (https://creativecommons.org/licenses/by/4.0/).

1. Introduction

Victor in [1] analyzed the feasibility of using a conventional induction machine as a split-winding bearingless motor. He performed position and current control of the machine; however, he observed that radial position control was not satisfactory for speeds below the rated limit. In recent years, Ref. [2] studied the replacement of PID controllers for radial position control with controllers based on fuzzy logic. Noting the strong nonlinear and parameter-varying characteristics of induction motor bearings, he analyzed the contribution of Fuzzy controllers on transient and permanent regime performance. In order to reduce the number of equipment needed for machine control, Ref. [3] optimized the structure of the motor bearing by proposing a new way to connect the coils in the machine stator. In [4], the machine's performance operation with a conventional state estimator and a neural state estimator was compared.

Speed control operating with the bearing motor was studied by [5,6]. The Artificial Neural Networks (ANN) technique was chosen. The ANFIS technique was investigated and studied by [7–9]. The adaptive neuro-fuzzy in motor studied by [10,11]. The speed control

operating with the bearing motor was evaluated by comparing the implementation of classic PI control with an artificial intelligence technique. Thus, the Artificial Neural Networks (ANN) technique was chosen to replace the classic PI control technique. The first step in implementing ANN was choosing the data set, the ANN input data are the mechanical speed and the mechanical speed error. The ANN output data is the torque current.

This work aimed to study and implement the artificial intelligence technique applied to vector speed control for the split wound type bearing motor based on the induction motor. The aim was to investigate and simulate the intelligent ANFIS techniques and Neural Networks to evaluate the performance of the motor-bearing in the following conditions: operating as an estimator and as a speed controller. In the experimental part, the TMS3208F28335 DSP was used to integrate the control algorithm with the current, position, and speed interfaces, by composing a cascade system. The intelligent technique implemented was the Neural Network, which acted as a speed controller. The position and mechanical speed results were compared with the PI speed controller and the Neural Controller. The control algorithm implemented in the TMS320F28335 DSP was developed in ANSI C programming language. The motor-bearing system is located in the Computer and Automation Engineering Laboratory (LECA) at UFRN.

On the other hand, we have the following articles. In [12], it is presented that crack is a common fault of rotor systems. The research on crack fault detection methods is mainly divided into numerical and experimental studies. In [13], the article classifies the dynamic response of rolling bearings in terms of radial internal clearance values. The value of the radial internal clearance in rolling-element bearings cannot be described in a deterministic manner, which shows the challenge of its detection through the analysis of the bearing's dynamics. In [14], it is presented that traditional machine learning prediction methods usually only predict input parameters through a single model, so the problem of low prediction accuracy is common.

The article describes the implementation details of controllers that provide the operation of the bearing motor. The system is made up of current, radial rotor position, and speed, which operate in a cascade. Control loop implementations started with the loop from the innermost (fastest) control to the outermost (slowest) loop, following the sequence: current control, position control, and speed control. Speed and position controllers are responsible for the generation of reference currents for current control. Other articles dealing with the topic of Bearingless Induction Motor are listed below [15–20].

The article has the following sections: In Section 1, the introduction is presented. In Section 2, simulations of the techniques of Artificial Intelligence are presented. In Section 3, the design and analysis of the ANFIS System is presented. In Section 4, neural controller design and analysis are presented. In Section 5, the Experimental Arrangement is presented. In Section 6, the control structure in the bearing motor cascade is presented. In Section 7, position control is presented. In Section 8, radial forces generation is presented. In Section 9, experimental results are presented. Finally, in Section 10, it is presented conclusions.

2. Simulations of the Techniques of Artificial Intelligence

This section introduces vector modeling of the induction machine working as a bearing motor. The characteristics have detailed the design of the Neuro-Fuzzy Estimator and the Neural Controller. The results showed a good performance for the two applied techniques: as an estimator and as a speed controller, both of them are models of the induction motor operating as a bearing motor.

The evaluation of artificial intelligence techniques uses the diagram of blocks of Figure 1. The neural controller replaced the green block represented by the Proportional-Integral, and the estimator conventional represented by the orange block by ANFIS.

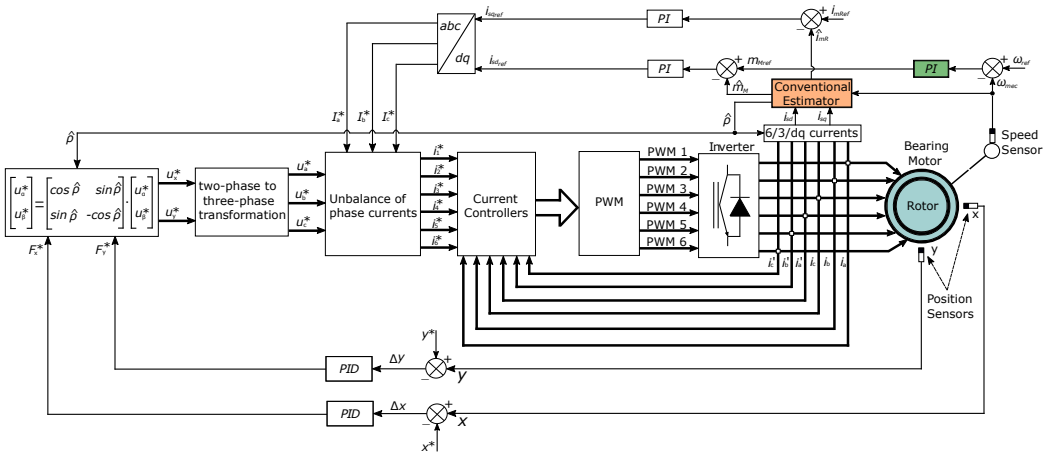


Figure 1. Block diagram of the proposed simulated system.

The block diagram in Figure 1 presents the system's complete structure adopted in the computer simulation stage. The modeling described in the next section and the other topics describe the main parts, requirements, and restrictions for the system to function as a bearing motor (blue block).

2.1. Three-Phase Induction Bearing Motor with Coil Divided

The proper operation of a bearingless machine requires control of the position, rotation, and torque of the rotor shaft. Table 1 presents some parameters obtained through tests performed in the laboratory [1] and adopted in this work for the simulations and obtaining the results.

Table 1. Motor Parameters and Characteristics.

Symbols	Description	Values
Pnom	Rated power	3.70 kW
Wmec	Rated Speed	1715 RPM
Tnom	Rated voltage	380 V
Np	Pole Pair Number	2
R1	Stator Resistance	1.182 Ω
R2	Rotor Resistance	1.42 Ω
J	Inertia moment	0.00995 kg·m^2
Ls	Stator Inductance	6.56 mH
Lr	Rotor Inductance	6.56 mH
Lm	Magnetization Inductance	0.14 H
r_{fe}	Core loss	891.2 Ω
g_0	Gap size	0.25 mm

The machine's structure adopted as a reference in this work has three phases, four poles, and utilizes the squirrel cage rotor; the coils are connected in series to form a phase group, and each phase group has two diametrically opposite coils, according to Figure 2. Figure 2 shows the distribution of the coils in the stator and the currents in each half group of the winding for the bearing motor used in the research. Figure 2 shows the stator winding distribution, where there is a 120° phase shift angle between each phase group axis. Figure 2 below describes the unbalance of the currents for the position control. In order to reduce the system's complexity, it was considered that the rotor be centered for the simulations. Note that i_{a1} is the stator current, and i'_{a1} represents the rotor current.

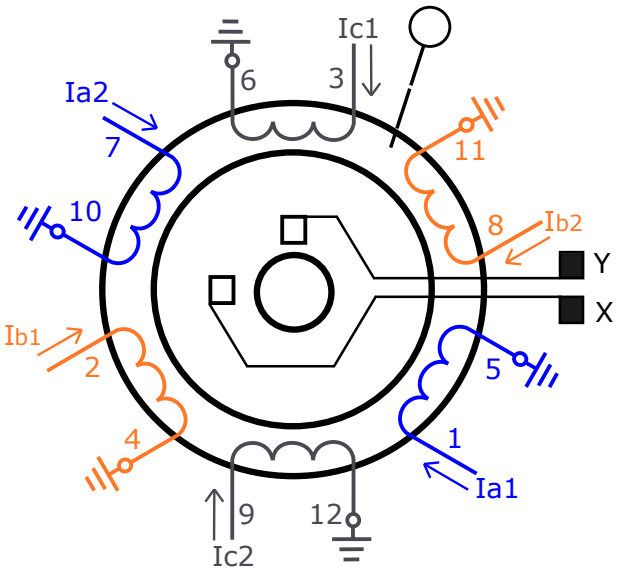


Figure 2. Stator coil layout.

2.2. Description of Artificial Intelligence Techniques Applied to the Bearing Motor

The implementation of artificial intelligence techniques took into account consideration of some criteria for the simulation. Use MATLAB for the implementation of the proposed system in Figure 1.

2.3. ANFIS Estimator

The conventional estimator adopted in the simulations was compared with the ANFIS estimator, and the training process using a 60-s training time interval, and variations of parameters were imposed considering the following criteria:

- Successive ascending and descending steps were applied between 0 and 2000 rpm (reference speed ranges);
- Variation of rotor time constant (every 2 s, so random values ranging from 0–20% concerning the nominal value of the constant);
- Every 5 s, increasing and decreasing variations were applied load of 0.05 N·m (load torque variation); This criterion was based in [21].

2.4. Neural Controller

The Neural Controller replaces the PI Speed controller in Figure 1. The data collection for training the neural network followed some criteria:

- The training process used a training time interval 60 s;
- Successive ascending and descending steps were applied between 600 and 1900 rpm (random variations of reference speeds);

3. Design and Analysis of the ANFIS System

The structures adopted in the Neuro-Fuzzy estimator were based on two estimators, one for estimating the magnetizing current and the other for estimating the rotor flux. The ANFIS 1 estimator uses the following inputs: the direct field current i_{Sd} and the delayed magnetizing current, and as output, the magnetization current. The ANFIS 2 uses the following inputs: mechanical velocity quadrature current i_{Sq} angular velocity as output estimated after discretization $d\hat{\rho}$.

In order to find the best configuration, it was performed several training with different parameters to obtain better criteria for the simulations according to Tables 2 and 3.

Table 2. ANFIS 1 Parameters.

Pertinence Functions	Epoach	Training Error	Validation Error
2	50	0.0558002	0.00813261
3	150	0.0488926	0.00815185
3	300	0.0409925	0.01109080
5	500	0.00175787	0.00781050

Table 3. ANFIS 2 Parameters.

Pertinence Functions	Epoach	Training Error	Validation Error
2	50	0.00406290	0.00489893
3	150	0.00533958	0.7491140
3	300	0.00448118	0.3522810
5	400	0.00359959	0.3302490

The criteria adopted in both estimators were 300 times for training and zero-tolerance error.

Figure 3A illustrates the Fuzzy surface obtained as a result of quadrature and magnetization current training. It is deduced that the linear result obtained is due to the centered rotor. Figure 3B illustrates the Fuzzy nonlinear surface obtained due to speed training mechanics and quadrature current.

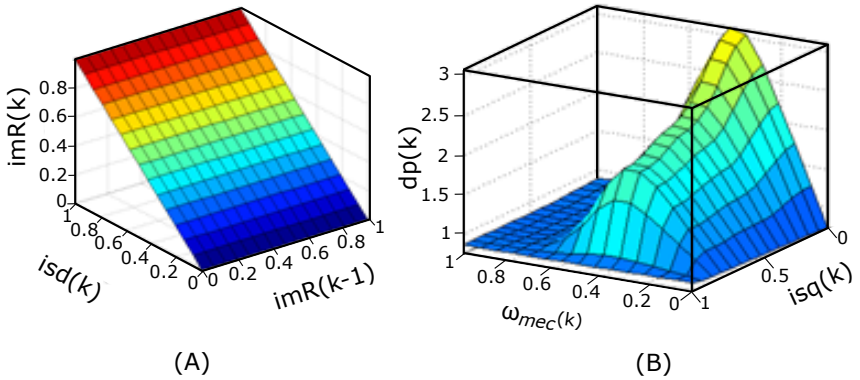


Figure 3. (**A**)—Fuzzy Sugeno Surface—ANFIS 1 and (**B**)—ANFIS 2.

Figure 4 illustrates the behavior before and after training to adjust the memberships: i_{Sq} and i_{mR} the curves [blue, green and red] represent the rules generated by ANFIS and {in1mf1, in1mf2 and in1mf3} are the memberships generated by ANFIS 1 and by ANFIS 2 are {in2mf1, in2mf2 and in2mf3}.

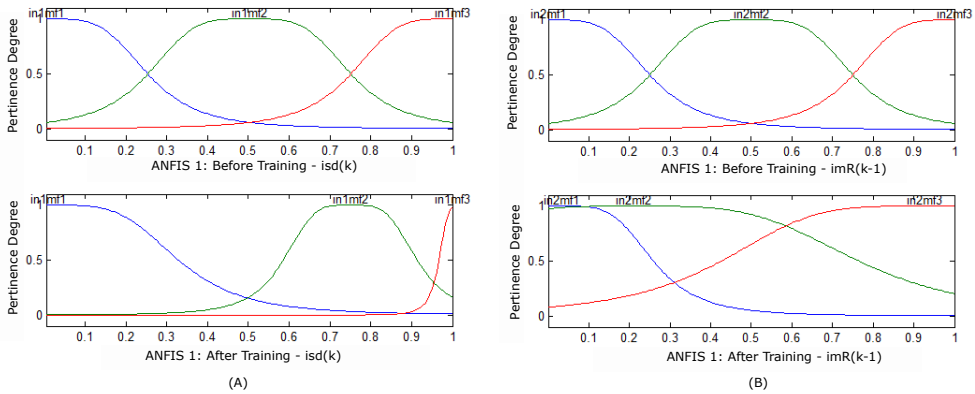


Figure 4. (**A**) Pertinences before training and after $-i_{Sd}(k)$; (**B**) Pertinences before training and after $i_{mR}(k-1)$.

It is observed that after the end of the training, the pertinence functions of Figure 5 were adjusted for each input of estimator 1 of Figure 3A. With the result of the training of the ANFIS 2 estimator, the membership settings for the entries were obtained. Figure 5 illustrates the behavior before and after mechanical speed training.

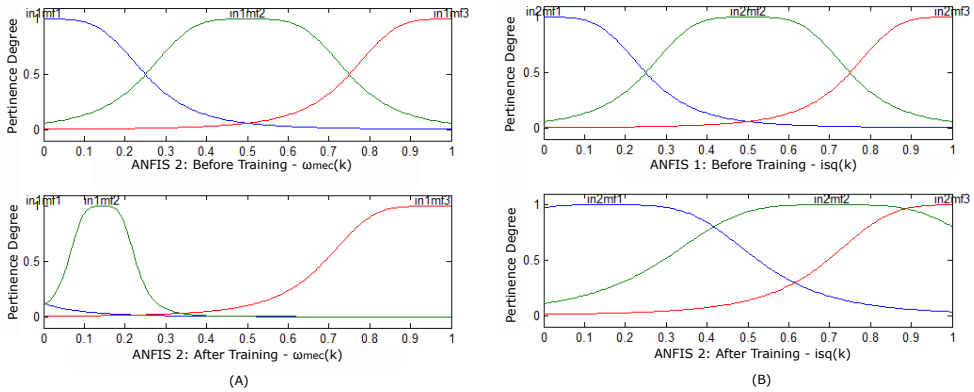


Figure 5. (**A**) Pertinences before training and after $-\omega_{mec}(k)$; (**B**) Pertinences before training and after $i_{Sq}(k)$.

Figure 5A shows the cancellation of membership already in Figure 5B there was no cancellation of membership, but a distribution of the same. These elimination and distribution results are pertinent to the Neuro-Fuzzy training.

Results of Simulations with the ANFIS Estimator

The simulations were run in the range of 0 to 20 s. The result shown in Figure 6 shows the mechanical speed of the motor simulated subject to the following reference changes 680, 1800, and 900 rpm, and then a perturbation at the instant 10 s is applied. The disturbance was an application of a load torque with a nominal value of 5.4 N·m.

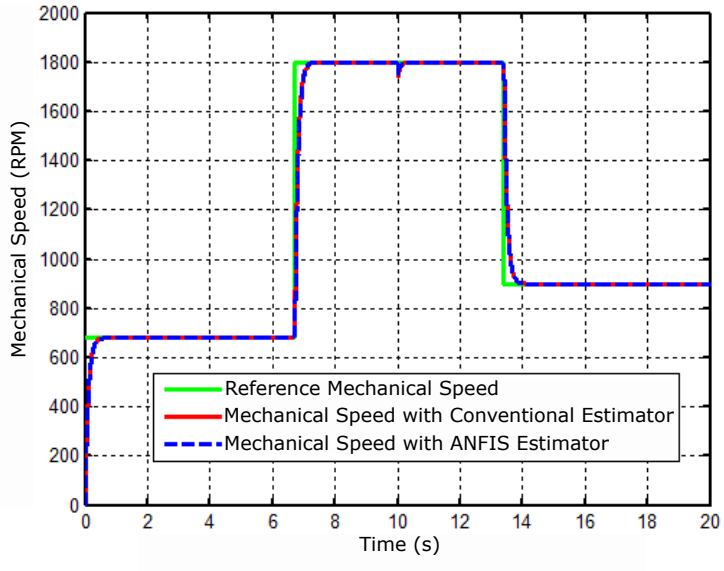


Figure 6. Comparative result of mechanical speed with estimators.

Figure 7 shows the behavior of the electrical torque in the conditions imposed in the simulation with conventional estimators and with the Neuro-Fuzzy estimator.

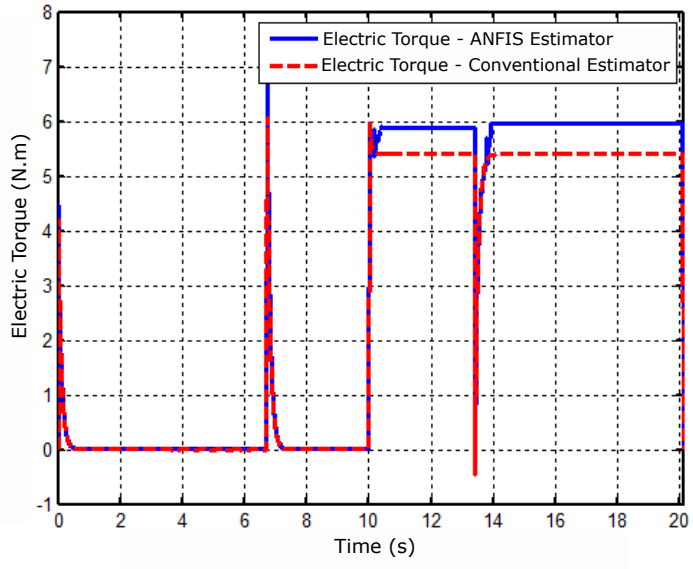


Figure 7. Electrical torque response operating under simulation conditions.

Figure 8 shows the behavior of the angular position with a zoom in an operating range of 0 to 0.2 s, which is observed in these results from the $\rho(k)$ timing for the estimators.

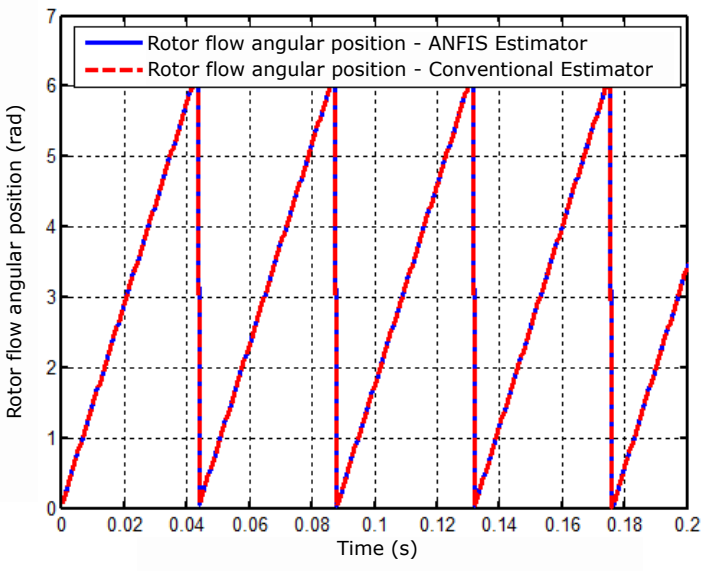


Figure 8. Angular position result of the rotor flux.

4. Neural Controller Design and Analysis

The neural structure used the three inputs: mechanical speed—wmec(k), error(k) current error; and the previous error (k-1) and as an output torque reference (nM_{ref}) for the torque controller. The process of training was carried out in offline mode, and its collection used 12,000 points for the input and output pairs, with a mechanical speed variation of 600 to 2000 rpm, randomly. Table 4 presents the parameters structures of the Neural Network, in which the convergence of the training process occurred in 841 epochs.

The topology in Table 4 was chosen after several performance tests with a different number of layers and neurons per layer, the algorithm of chosen training was the Levenberg–Marquardt. Figure 9 shows the error curve obtained with network training neural.

Table 4. Neural Network Parameters.

Network Architecture	Multilayer Perceptron
Training type	Supervised-offline
Layers number	3
Input layer neurons	3
1st hidden layer neurons	10
Output layer neurons	1
Training algorithm	Levenberg–Marquardt backpropagation
Learning rate	5×10^{-2}
Epochs number	841
Training error	9.4197×10^{-7}
Hidden layer activation function	Hyperbolic tangent
Output layer activation function	Linear

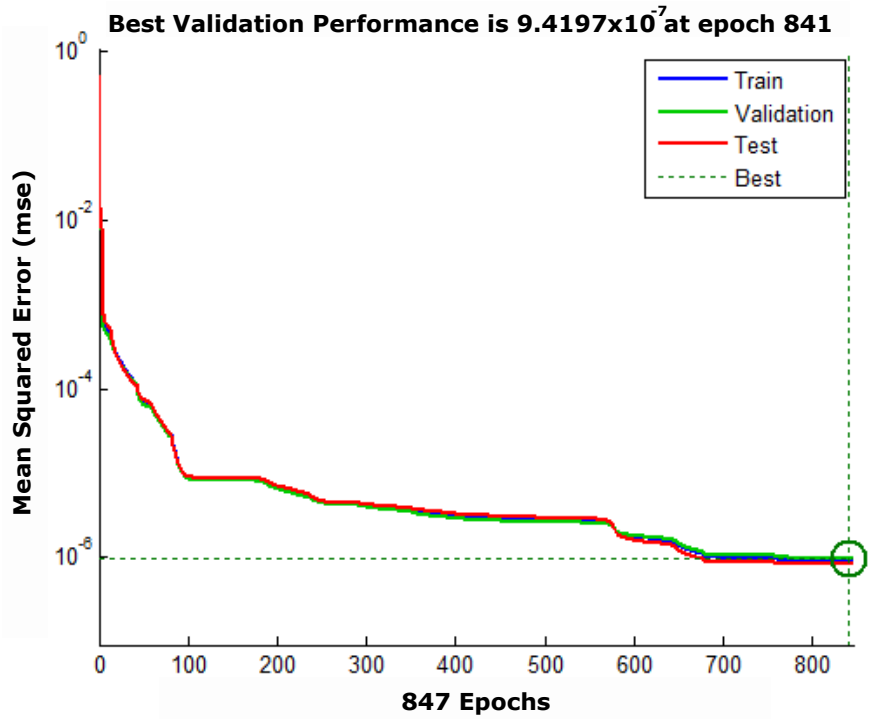


Figure 9. Mean squared error for training (9.4197×10^{-7}) with 847 epochs.

Figure 10 shows the performance of training, validation, and assessed tests resulting from the training.

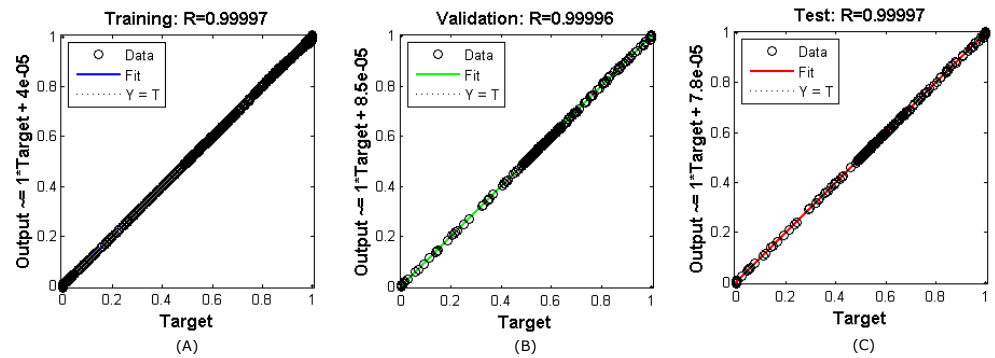


Figure 10. Results of training (**A**); validation (**B**); and Neural Network tests (**C**).

Figure 10 shows the R parameter at the top. This parameter indicates the relationship between the output and the target, varying between 0 and 1. The closer to 1, the better the prediction. After training, the weights were adjusted, and the neural network simulation replaced the PI control in Figure 1.

Results Neural Network Simulations

The simulations were run from 0 to 10 s. The results shown in Figure 11 show the mechanical speed of the motor simulated subject to the following reference changes: 1200, 1800, and 1500 rpm.

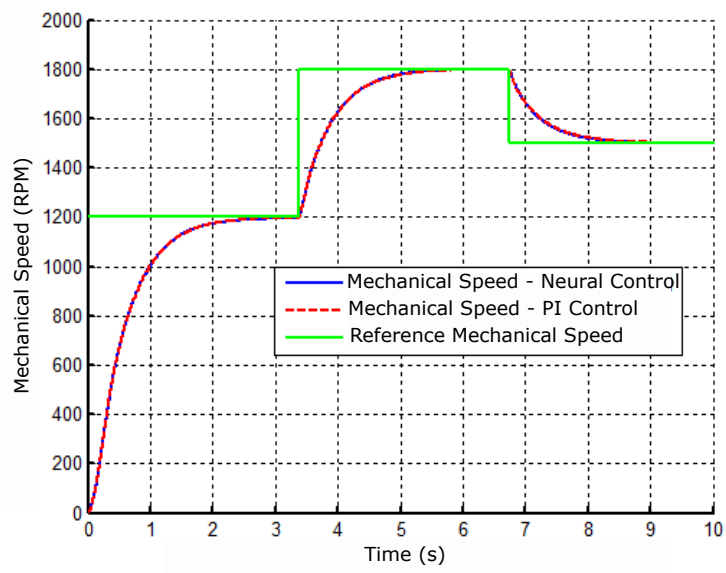


Figure 11. Comparative result of the mechanical speed with the controllers: neural and PI.

Figure 12 shows the behavior of the angular position with a zoom-in operating range from 0 to 0.4 s. It is observed in these results that the $\rho(k)$ timing for the estimators.

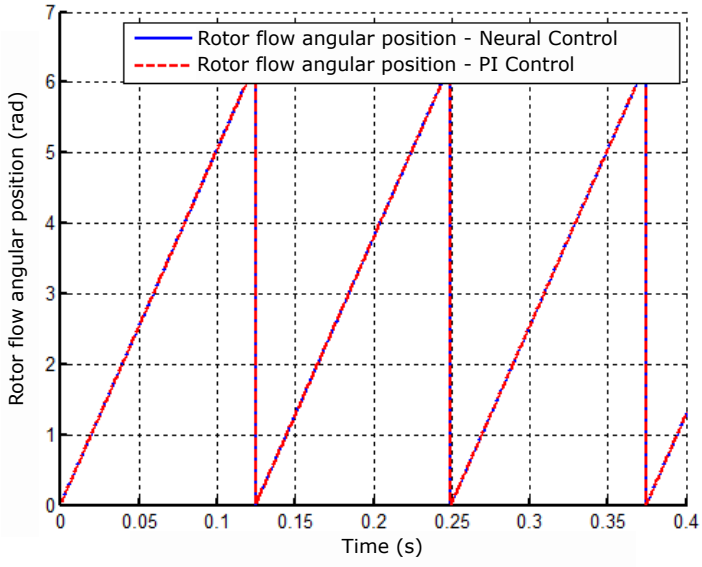


Figure 12. Angular position result of the rotor flux with the neural controller and PI of velocity.

5. Experimental Arrangement

The 3.7 kVA three-phase induction motor received modifications to operate a bearing motor; for example: the configuration of the double star coils and the removal of one of the bearings from one end of the rotor shaft. This last modification caused problems in the work of [1], according to which the problem of eccentricities of the motor-bearing shaft caused when there is displacement of the rotor made it difficult to adjust the position controller gains. The orbits were designed by rotating the shaft manually and then translating it through the periphery of the air gap. According to [1], after installing the self-aligning bearing, the shaft started to produce several orbits when peripherally displaced. Figure 13 shows three possible orbits designed by moving the shaft peripherally in the housing box of the top bearing.

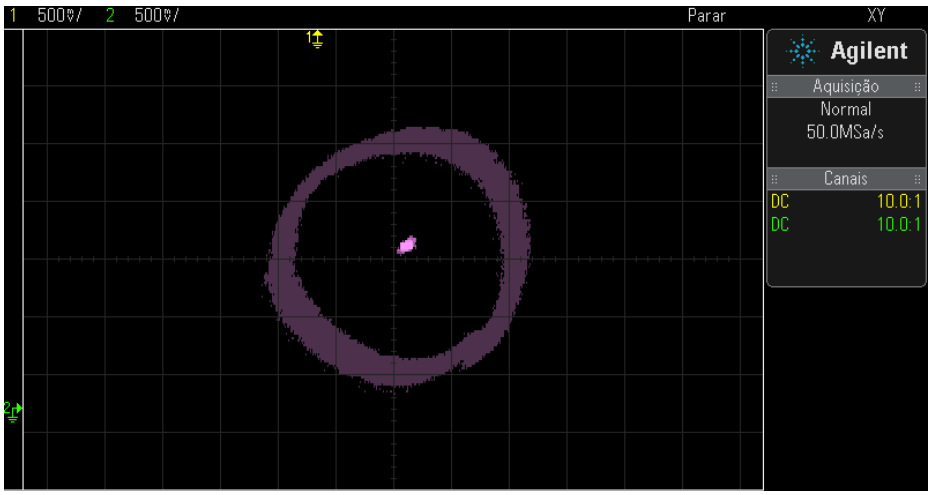


Figure 13. Motor-bearing shaft eccentricities.

After replacing DSP 2812 with DSP 28335, the empirical tuning of the Position PD controller was a difficult task. In order to correct the imbalance, the induction motor was disassembled, and the rotor shaft composed of the bearings and the disc was positioned in the lathe to perform roughing on the disc. In order to increase accuracy, the clock was used in thinning.

However, the eccentricity problem persisted, decreasing only the number of orbits. With the correction of the unbalance of the shaft in the lathe, the number of orbits went from three to two. This phenomenon made it difficult to tune in to the position controller. The solution found was the replacement of the conventional induction motor modified by the prototype of the bearing motor used, which was located in the Laboratory of Computer Engineering and Automation (LECA) at UFRN.

The bearing motor is a conventional induction machine adapted to operate without its mechanical bearings, having its radial positioning controlled by magnetic fields. The data used as parameters for the control of the machine were from the Table 5.

Table 5. Motor prototype parameters.

Parameters	Values
Rated power	1 Hp
Frequency	60 Hz
Poles numbers	4
Rated voltage	220/380 V
Rated current	3.02/1.75 A
Empty current	1.90 A
No load power	160.00 W
Resistance	7.38 Ohms
Stator Resistance per Phase	0.73 Ohms

After the replacement of the motor, it was necessary to configure the connection of the electric motor. For this, the coils and they were respective phases, because, the stator coils suffered some changes, they were divided in half as a strategy to carry out of control. In Figure 14, the location and identification of the groups of coils.

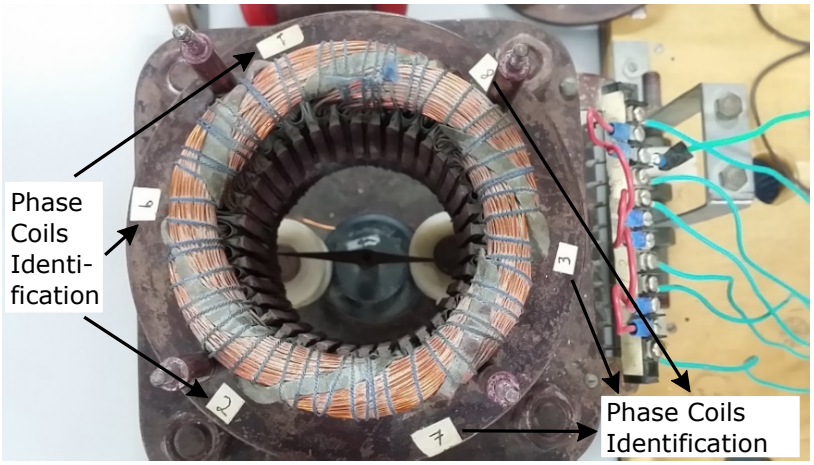


Figure 14. Coverless bearing motor with identification of the coil groups.

Based on the experiments, Figure 15 shows the arrangement of connections of these windings for operation as a bearing-less machine of the split coiled.

In order to facilitate the identification of phases and coil groups for name the *X* and *Y* axes for position control, it was necessary to perform two experiments with the aid of a compass. It is possible to check the compass orientation indicating the *Y* direction, shown in the Figure 16.

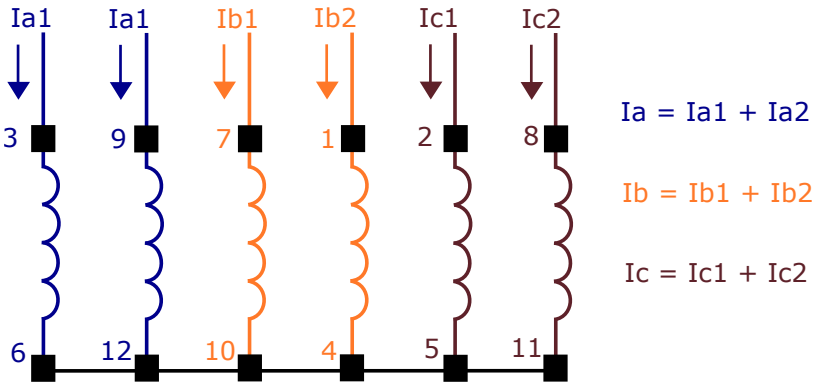


Figure 15. Motor-bearing winding connection arrangement.

The results of Figure 16 identified each coil group according to the sequence of Figure 15. For this, each group of coils was excited with continuous tensions.

However, it was necessary to adjust the position and speed of the related peripheral to allow effective control under the conditions imposed on the bearing motor. These modifications are presented in the following sections.

5.1. Radial Position Sensors

The radial position control for a bearing motor consists of making the rotor float; that is, without mechanical contact with the stator. Another advantage identified in replacing the bearing motor was the increase in the air gap, which went from 0.3 mm to 0.5 mm, which allows a larger range for empirical tuning of position control.

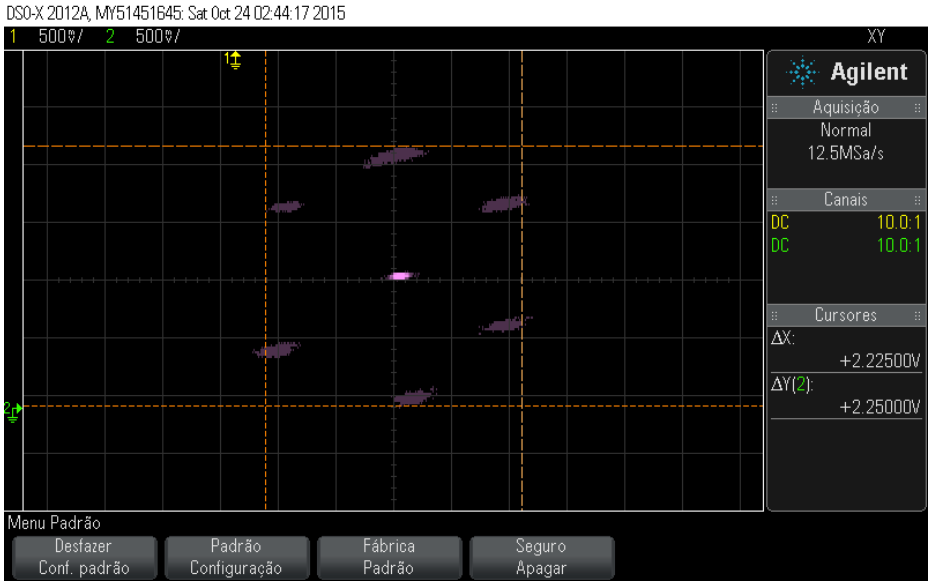


Figure 16. Bearing motor winding connection arrangement. The result identified each coil group according to the sequence of Figure 15.

5.2. Rotation Sensors

A rotating machine, when subjected to a torque on the shaft, in addition to needing more current in the coils, it also undergoes a variation in rotation. Thus, it is essential to know the rotation in real-time and the currents in the coils to implement a control machine rotation. In order to measure the rotation on the axis of the bearing motor, an encoder consisting of a disc was adopted uniformly perforated, a receiving transistor, and a light-transmitting LED structured infrared.

Among the peripherals that make up the bearing motor, such as those that were used in [1].

5.3. Complete System

The modulation of current in frequency inverters is performed through signals from the DSP control system. The current produced generates both torque and radial forces from rotor positioning. The mechatronic system, including each of the elements composed by the system and other components such as interfaces, sensors, and command devices, can be seen in Figure 17.

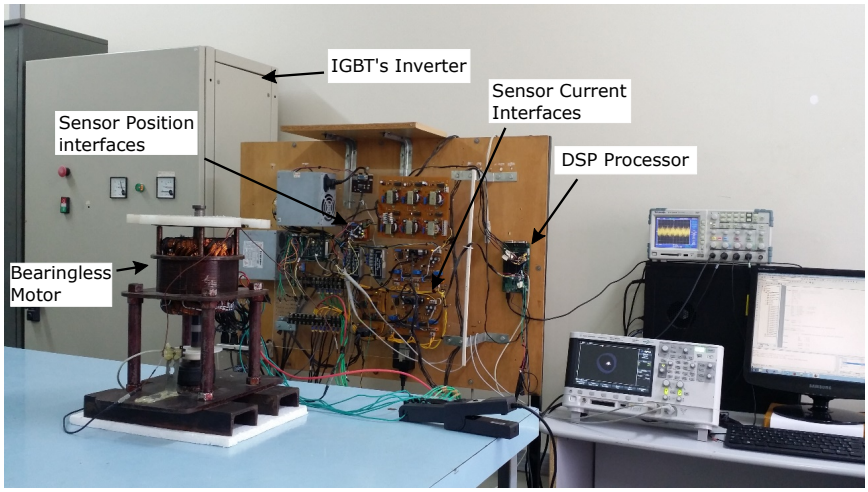


Figure 17. Mechatronic system with interfaces and the bearing motor.

This section dealt with the details of the changes made to the interfaces with the bearing motor. Basically, there were changes in the position and velocity sensors, and after adjustments, the system was able to implement the control structure and obtain the experimental results, which are exposed in the following section.

6. Control Structure in Bearing Motor Cascade

The following text describes the implementation details of the controllers that provide the operation of the bearing motor. The complete system comprises the current, position, and speed controllers, which operate in a cascade. The implementations of the control loops were started with the loop. from the innermost (fast) control to the outermost (slower) loop, following the sequence: current control, position control, and speed control. The speed and position controllers generate reference currents for current control. So after the action of controlling the currents of each coil is applied to the motor-bearing windings, the scalar PWM outputs are generated for the two three-phase inverters.

Current Control

The high performance in the drive of electrical machines depends mainly of the control technology implemented, being employed control techniques with current feedback in all applications. These techniques require fast response, high accuracy, and a performance high level. Current sensors, as well as other sensors used in the machine are important for the control in real-time, can impose changes necessary for the correct functioning of the machine. Current controllers must be of the Proportional-Integrative type (PI), they are simple to implement and manage to eliminate errors in regime [1]. The structure used for the control of current in this work was based on the module implemented by Texas (C28x Solar Library [22]). This module has the following characteristics: programmed output saturation; adjustment of independent weights on actions proportional and derivative; reset in anti-windup integrator; and a filter Programmable for a derivative action. However, the derivative action was annulled for this control, acting only on the proportional and integral actions.

The equation of the PID controller before saturation is described as Equation (1):

$$v_1(k) = K_p[u_p(k) + u_i(k) + u_d(k)] \tag{1}$$

Each term can be written as follows: Proportional term:

$$u_p(k) = K_r r(k) - y(k) \tag{2}$$

Integral term:

$$u_i(k) = u_i(k-1)K_i[r(k) - y(k)] \tag{3}$$

Derivative term with filter:

$$u_d(k) = K_d[c_2 u_i(k-1) + c_1 e(k) + c_1 e(k-1)] \tag{4}$$

Finally, the output with saturation is defined:

$$u(k) = \begin{cases} U_{max} : v_1(k) > U_{max} \\ U_{min} : v_1(k) < U_{min} \\ v_1(k) : U_{min} < v_1(k) < U_{max} \end{cases} \tag{5}$$

In these, $r(k)$ a reference; $y(k)$ a control variable; $u_d(k)$ term derivative; $u_i(k)$ integrative term; $u_p(k)$ proportional term; K_r, the weight referring to reference; K_p the proportional gain; K_d the derivative gain; c_1 the derivative filter coefficient 1; c_2 the coefficient of derivative filter 2; U_{max}, the maximum saturation limit; U_{min}, minimum saturation limit.

The control laws of Equations (1)–(5) were implemented in DSP 28335. The implementation is obtained from Texas Instruments, [22]. Six PI controllers operate in a closed loop inside the DSP interrupt to control the bearing motor current.

7. Position Control

For the implementation of position control, you must take into consideration the study by [1,21]. These works demonstrate the rotor positioning model and identify that the model is unstable in open mesh due to the presence of two poles, one in each semi-plane. The solution found for the system to become stable was the implementation of the Proportional-Derivative (PD) controller, which adds a zero which is positioned to attract the place of the closed-loop roots to the left half-plane. The control law implemented for position control was based on [1].

8. Radial Forces Generation

Signals u_α, u_β come from the position control. Then, they undergo a rotational transformation to the static orthogonal system and transform into u_x, u_y and lastly there is a coordinate transformation biphasic to triphasic, resulting in u_a, u_b u_c, observed, that the controller signals u_a, u_b u_c, after the transformations, they have added to the phase current references or subtracted in each half group of coils from phases A, B, and C, respectively, to control the restoring forces of the rotor position, (Equation (6)).

$$\begin{aligned} I_1^* &= I_a^* + u_a \\ I_2^* &= I_a^* - u_a \\ I_3^* &= I_b^* + u_b \\ I_4^* &= I_b^* - u_b \\ I_5^* &= I_c^* + u_c \\ I_6^* &= I_c^* - u_c \end{aligned} \tag{6}$$

In these equations, I_a^*, I_b^*, and I_c^*, are the imposed phase reference currents and I_1^*, I_2^*, I_3^*, I_4^*, I_5^*, I_6^*, are the reference currents for position control. Due to the nonlinearity of the system, the tuning of the controllers becomes difficult to obtain; however, the parameters of the controllers were determined empirically.

Vector Speed Control

The speed controller used is a PI (Proportional-Integral) with anti-windup, the feature that interrupts the integration process when output has already reached a maximum saturation value [23]. For the implementation of velocity vector control; initially, the structure of control of Figure 18 using flow estimator. The big advantage of this structure using this estimator is the presence of a small number of equations, minimizing the computational effort [24].

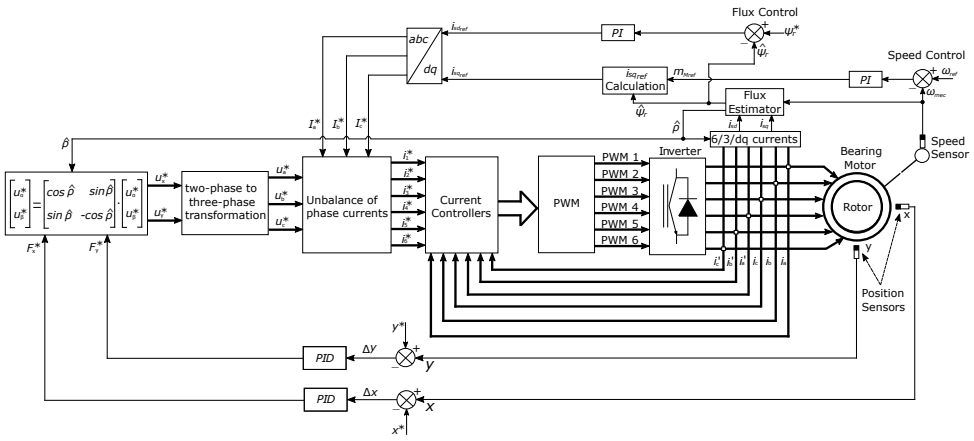


Figure 18. Control structure with flux estimator.

The flux estimator used in [24] is given by:

$$\hat{\lambda}_{est} = L_m i_{sd} \tag{7}$$

In this, $hat\lambda_{est}$, L_m the estimated flux; i_{sd} the mutual inductance.; i_{sd} the field current. Equation (7) is calculated from the field current i_{sd} and the inductance mutual L_m. Thus, the calculation of the torque current (i_{sq}) obtained from the Equation (8).

$$nM_{ref} = \frac{PL_m}{L_r}\lambda_r i_{sq} \tag{8}$$

here, nM_{ref} reference torque; L_r the inductance of the rotor; λ_r, the flux reference rotor; and P, the number of pole pairs. However, this structure was chosen for the following reasons: the difficulty of tuning in empirically the control loops, which consumed more time, and the fact of not having the necessary machine parameters to be used in Equations (7) and (8).

However, it was thought to obtain the parameters from laboratory tests, which were discarded due to the following disadvantages: A delay in the digital implementation of the control structure may be a physical problem with the engine, generating more time for its solution or maintenance. Therefore, the control system implemented for the vector control of speed of Figure 19 took into account two simplifications: impose a reference field current to not implement flow control and eliminate the current torque calculation, causing the control output go straight into Park, and Clarke's inverse transforms as torque investigation will not be taken into account. The structure of Figure 19 has three loops, the outermost being the Proportional-integral (PI) speed control, which controls the rotor shaft speed from the sensed feedback and whose output is the torque current isq_{ref} the Proportional-Derivative Integral (PID) controller for the positions referring to the x and y coordinates of the rotor, since, in practice, the added integral action should decrease the regime error. Position control is classified as a regulator, unlike the current control system, which is classified as a follower. Therefore, the last control loop is the current one, the innermost one, and quick response, with PI controllers for the six stator windings.

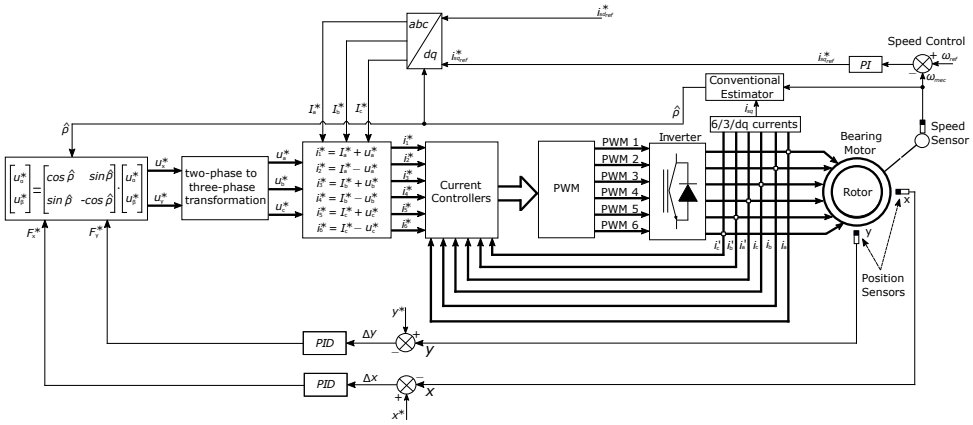


Figure 19. Bearing motor cascade control diagram.

This section allowed us to deduce the simplified control diagram and function for implementing velocity vector control. The choice is to discuss the current position and speed controllers that helped to define the chosen strategy. The next section presents the experimental results of each step of the cascade control loop of the bearing motor.

9. Experimental Results

The experimental results were obtained with the digital implementation of the control system in the motor-bearing using the DSP 28335. An artificial intelligence approach was implemented in the results of speed vector control. In addition, a comparison of the Proportional-integral velocity vector control with the neural controller.

9.1. Stator Currents

To validate the digital implementation of the current control, some experiments with the centralized rotor with the current PI control. The procedure followed the block diagram sequence in Figure 20, based on the block structure of Figure 19.

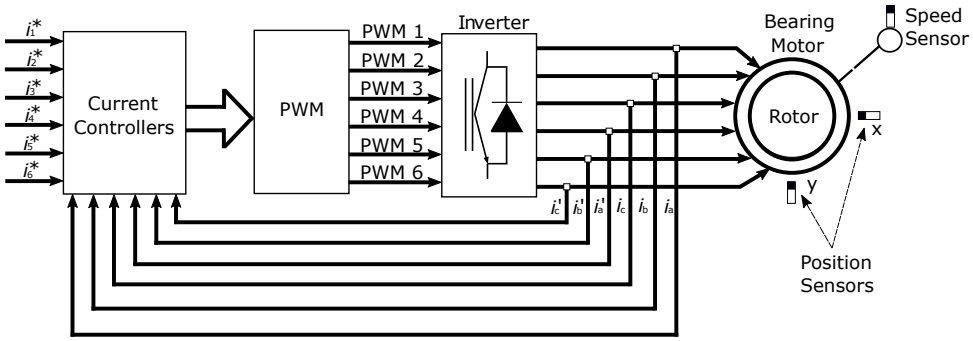


Figure 20. Motor-bearing current control.

Some experiments were carried out to validate the performance of the current PI controller. The first one was the response to several steps in the reference imposed on coil i_1 according to Figure 21. The PI controller parameters of current $K_p = 200$ and $K_i = 1.464844 \times 10^{-6}$ were empirically adjusted for obtaining the results and other experiments.

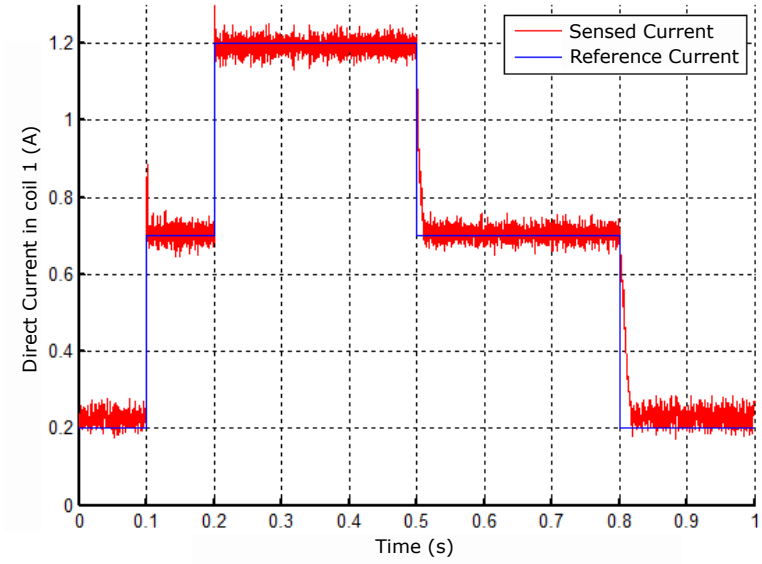


Figure 21. Response to the reference change in coil 1.

For this experiment, continuous currents were imposed with reference changes over 1 s interval of execution. Another result obtained was the current of sinusoidal reference, and we alternated it at a frequency of 60 Hz and with an amplitude equal to 1.5 according to Figure 22.

The experiments were carried out by changing the frequency and the reference range. Figure 23 shows the experiment obtained when the engine works at 15 Hz frequency with equal reference amplitude (Imax) to 0.8 A.

To evaluate the behavior of the bearingless machine operating as a induction and activating the six coils, it was necessary to perform two procedures: (1) fix the rotor shaft in the center so that it does not influence the dynamics of the experiment and operate with the rotor centered; (2) generate six streams of 120° offset references to generate the rotating field Equation (9).

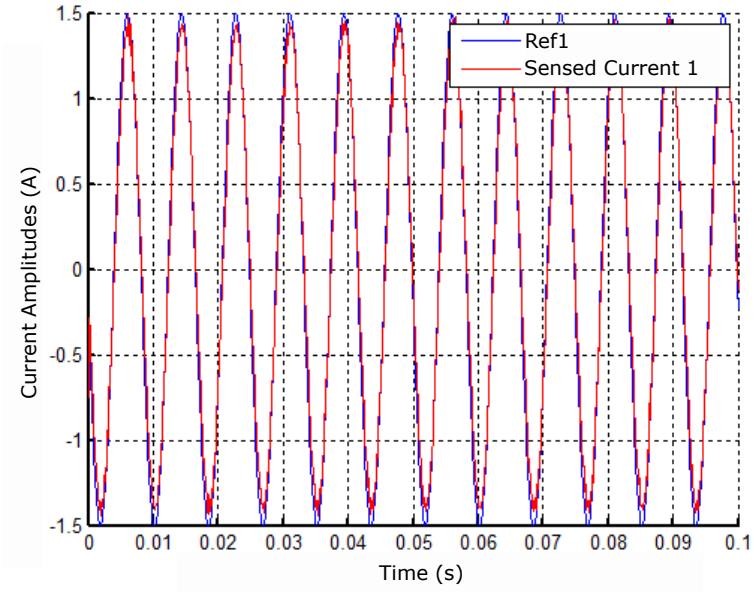


Figure 22. Response to sinusoidal reference in coil 1.

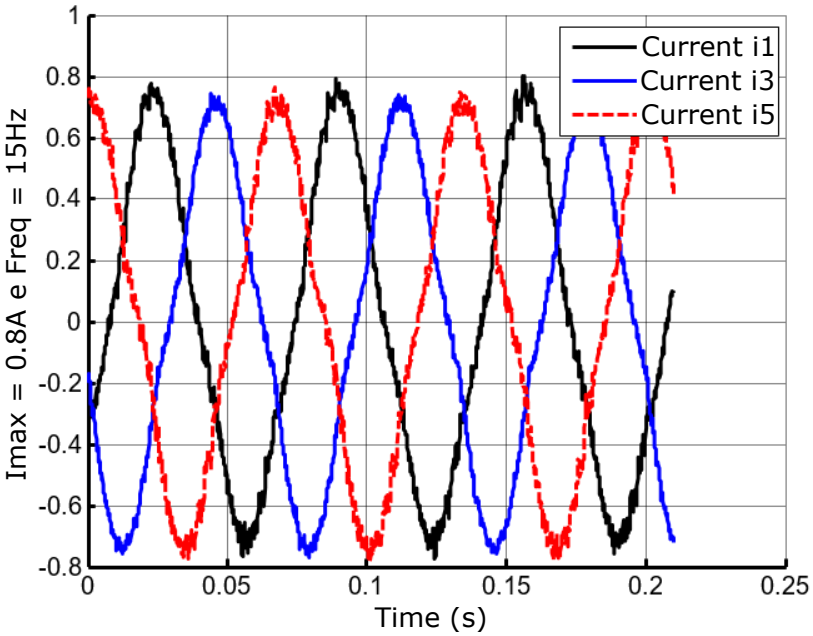


Figure 23. Lagged currents at 15 Hz frequency and 0.8 A amplitude.

$$\begin{aligned} i_1^* &= Imax * sin(wt + 0) \\ i_2^* &= Imax * sin(wt + 0) \\ i_3^* &= Imax * sin(wt - \frac{2\pi}{3}) \\ i_4^* &= Imax * sin(wt - \frac{2\pi}{3}) \\ i_5^* &= Imax * sin(wt + \frac{2\pi}{3}) \\ i_6^* &= Imax * sin(wt + \frac{2\pi}{3}) \end{aligned} \tag{9}$$

9.2. Radial Rotor Position

The results presented below were obtained with the control Proportional-Derivative-Integrative (PID) from some experiments. The results used the block diagram strategy of Figure 24 based on Figure 19.

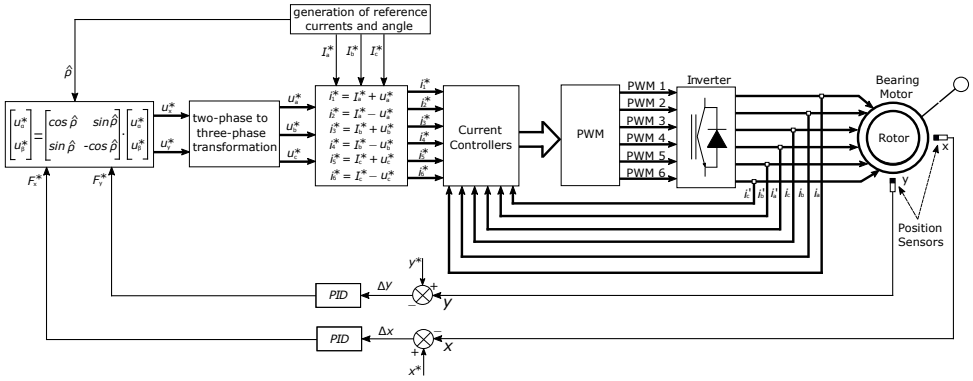


Figure 24. Cascade position control with motor-bearing current control.

After some empirical adjustments on the controller parameters, the gains obtained were: $K_{px} = 0.0005$, $K_{dx} = 0.028$, $K_{ix} = 1 \times 10^{-8}$, $K_y = 0.0005$, $K_{dx} = 0.06$, $K_{py} = 1 \times 10^{-8}$. An experiment was carried out with the controls of position acting independently, evaluating the behaviors of the X-axis and Y-axis. Figure 25 shows the response to a step variation for the position control along the X-axis.

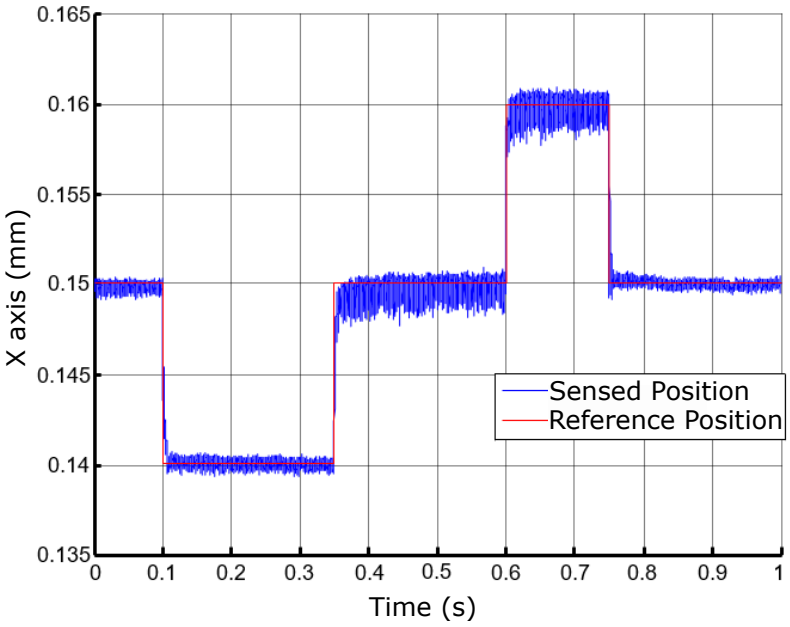


Figure 25. Position control results for the X axis.

Figure 26 shows the response to a step change for the control of position along the Y axis.

The results were collected in a steady state. The experiment performed operated at the frequency of 60 Hz according to Figure 27. The spot in the center of the figures represents the positions that the rotor has assumed in a given moment: the oscilloscope is in trace persistence mode.

In order to illustrate the dynamics of cascading control, the results considered an equal time window for the position controllers and the current operating at a frequency of 60 Hz. Figures 28–30 show the results of the cascading current and position controllers accordingly with the block diagram of Figure 24. The graphic of Figure 28A shows the reference currents, that is, the imposed currents I_a^*, I_b^*, and I_c^* for control of position, collected at an interval of 0.08 s.

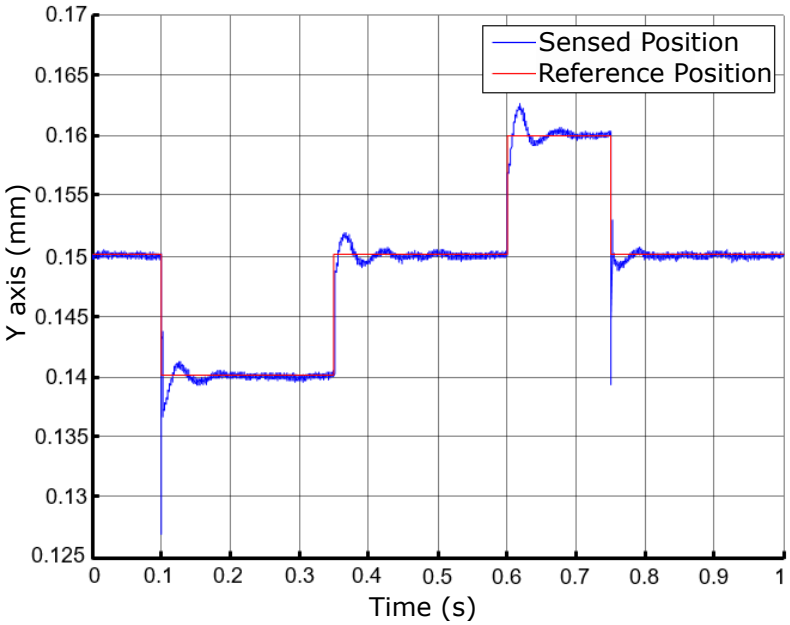


Figure 26. Position control results for the Y axis.

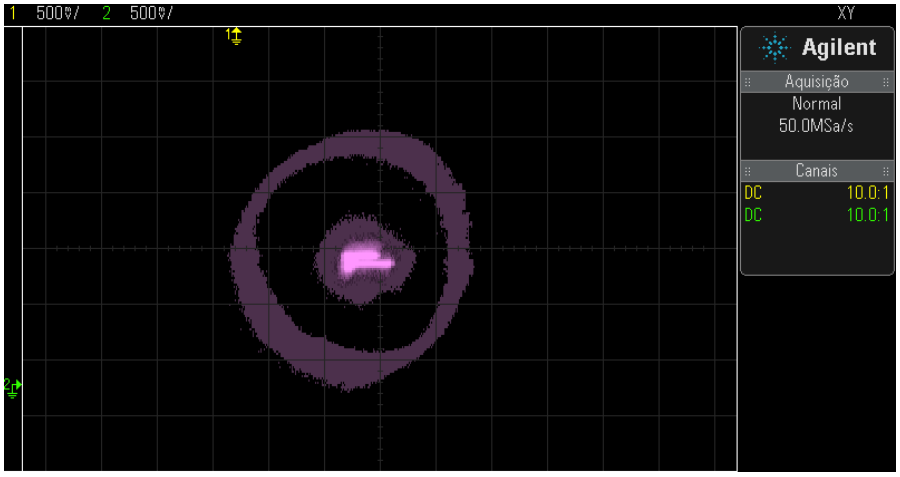


Figure 27. Position control results with a rotor scatter area for activation at 60 Hz.

The graph in Figure 28B, identified by the subtitles Ref1, Ref2 and Ref3, represents the composition of the reference currents I_a^*, I_b^*, and I_c^* with the signs from position controllers u_a^*, u_b^*, and u_c^*. Finally, the graph in Figure 28C represents the equivalent sensed currents in each phase. Figures 29 and 30 show the responses of the X and Y positions with their respective reading errors associated and control signals. There is a small change in the behavior of the sensed currents in Figure 28 at times close to 0.02 s, for example. This change is due to the control adjustment of the position of Figures 29 and 30 and observed in the control signals for the X and Y positions.

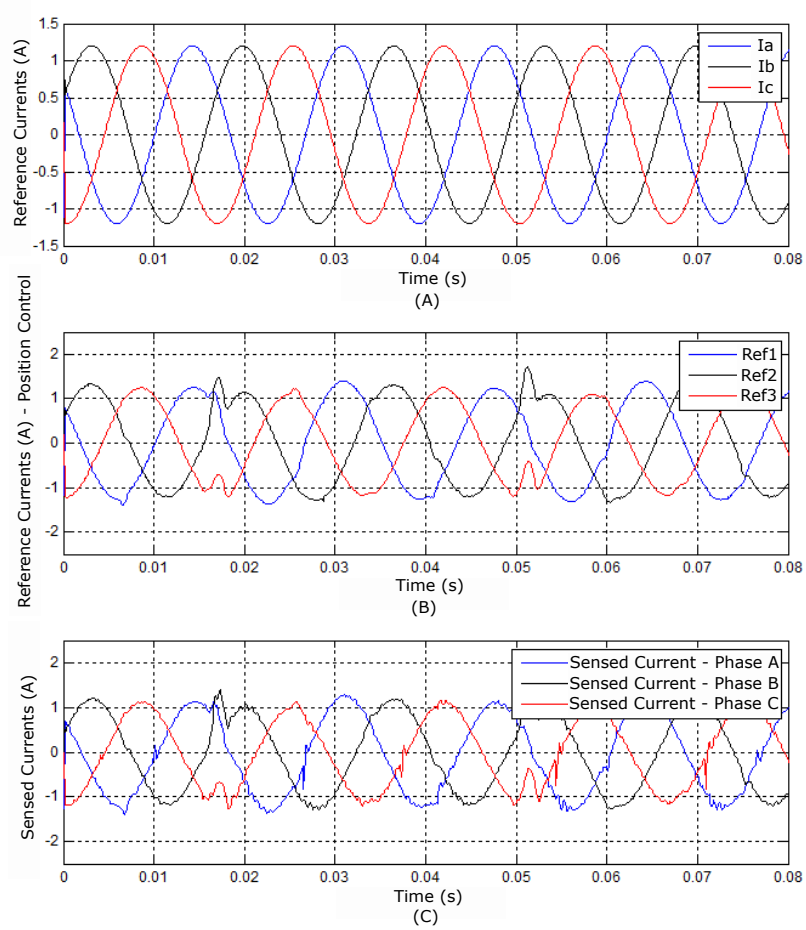


Figure 28. Results referring to (**A**) imposed, (**B**) controlled, and (**C**) sensed currents.

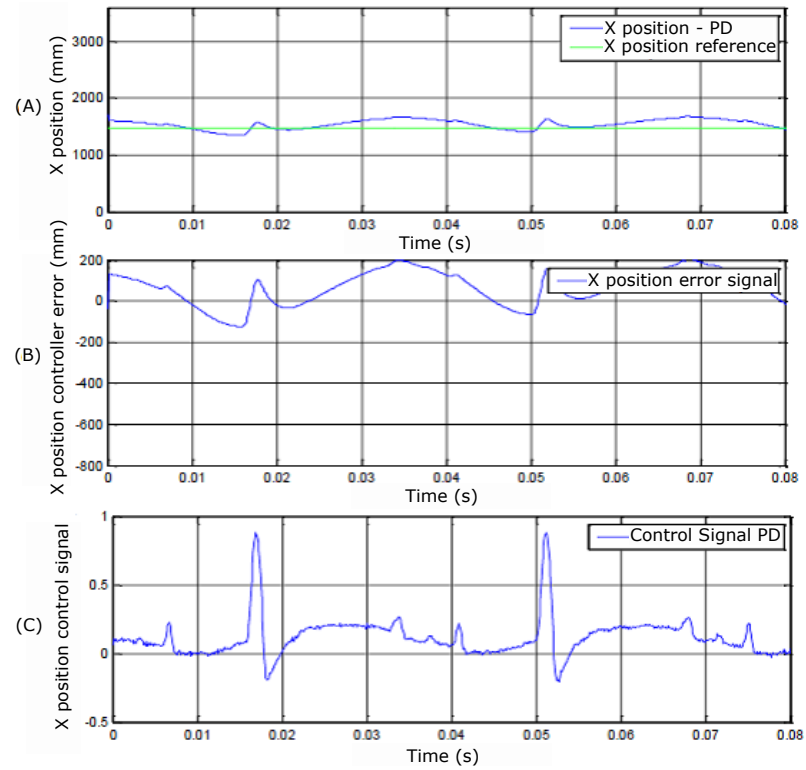


Figure 29. (**A**) *X* position, (**B**) controller error, and (**C**) control signals.

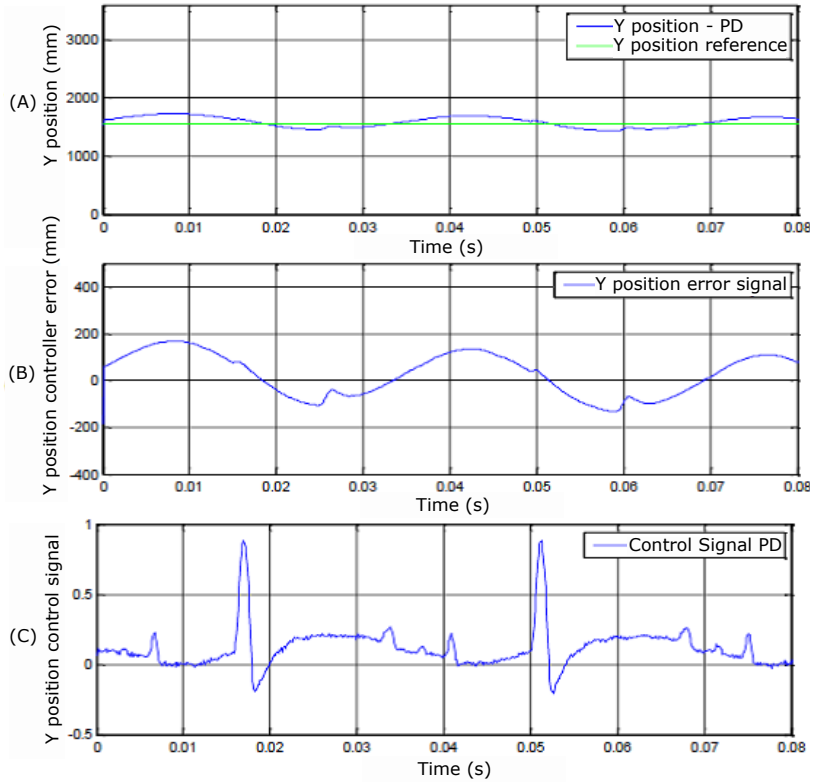


Figure 30. (**A**) *Y* position; (**B**) controller error; and (**C**) control signals.

9.3. Speed Control

The speed control operating with the bearing motor was evaluated by comparing the implementation of classic PI control with an artificial intelligence technique. The technique chosen was the Artificial Neural Networks (RNA) to replace the classic PI control. The ANFIS technique was investigated. However, due to the computational cost of its implementation, it was discarded.

The first step in implementing the ANN was choosing the data set for training and validation. The inputs are the mechanical speed (W_{mec}) the mechanical speed error $((Error_w))$ and the output is the current (Isq_{ref}). The input and output data pairs are used to adjust the internal parameters of ANN according to [25]. The RNA was configured fully connected. The database was developed with 20,200 samples, of which 70% of the data were used in training and 30% for validation. The training process was carried out in offline mode, and its collection used the input data with a variety of mechanical speeds randomly from 1% to 5% overrated speed 1800 rpm. Table 6 presents the structural parameters of the Neural Network, in which the convergence of the training process occurred in 104 epochs.

Table 6. New Neural Network Parameters.

New Network Architecture	New Multilayer Perceptron
Type of training	Supervised-offline
Number of layers	3
Input layer neurons	2
1st hidden layer neurons	10
Output layer neurons	1
Training algorithm	Levenberg–Marquardt backpropagation
Learning rate	5×10^{-2}
Epoch number	104
Training error	1.3909×10^{-5}
Hidden layer activation function	Hyperbolic tangent
Output layer activation function	Linear

The training algorithm chosen was the Levenberg–Marquardt, used in the Matlab toolbox for better accuracy; the topology Table 6 was chosen after several performance tests with a different number of layers and neurons per layer. The final choice led to considering the digital implementation and evaluating the processing time of the DSP. The more layers and neurons, the longer the processing time increases. Thus, the implemented structure analyzed the computational cost. Figure 31 shows the training performances, validation, and the evaluated test resulting from the training.

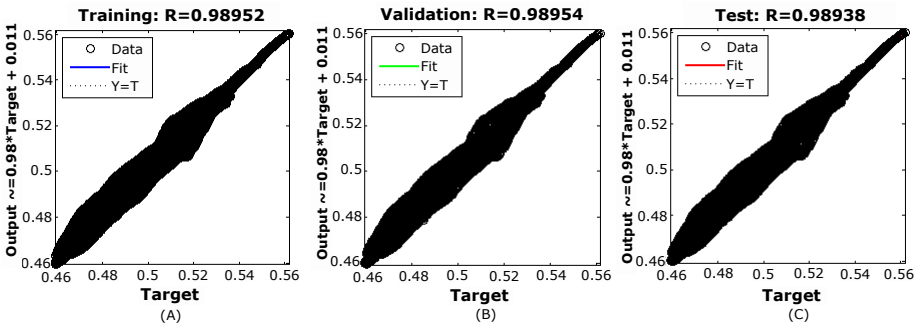


Figure 31. Result of training, validation, and testing of the Neural Network.

Figure 31 shows the R parameter at the top. This parameter indicates the relationship between the output and target, varying between 0 and 1. The more close to 1, the better the prediction. Figure 32 shows the training graph with the Mean Square Error (MSE).

After training, the weights and carried out two experiments to evaluate the functioning of the bearing motor operating with PI speed control with gains $K_{pw} = 0.01$ and $k_{pi} = 7.5 \times 10^{-5}$ and with the neural structure. The two case studies used the same RNA structure implemented.

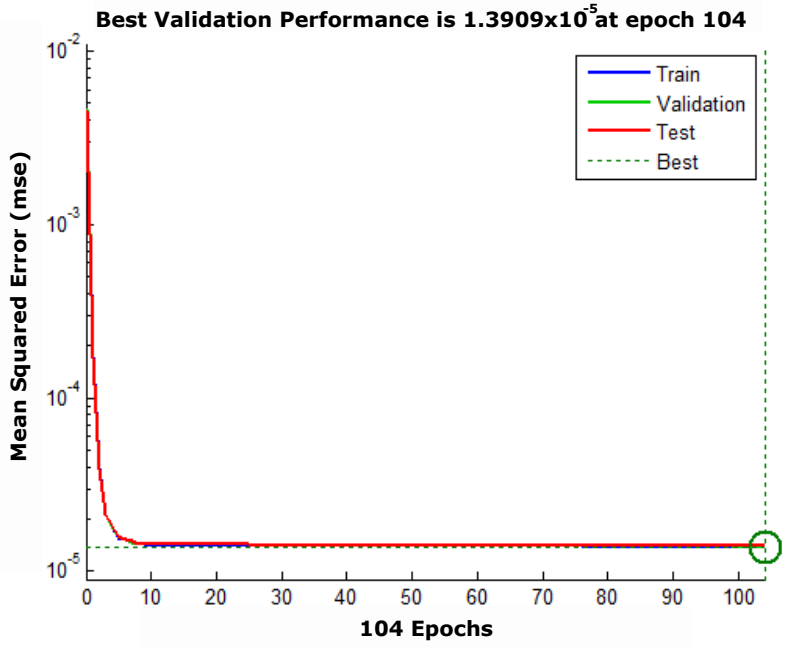


Figure 32. Mean squared error for training (1.3909×10^{-5}) with 104 epochs.

9.3.1. Case Study I—Ramp

The first experiment presents the system's behavior when being powered from rest to a rated speed of 1800 rpm. Figure 33 shows the mechanical velocity dynamics and the X and Y positions, respectively, in the function of time operating with the two controllers.

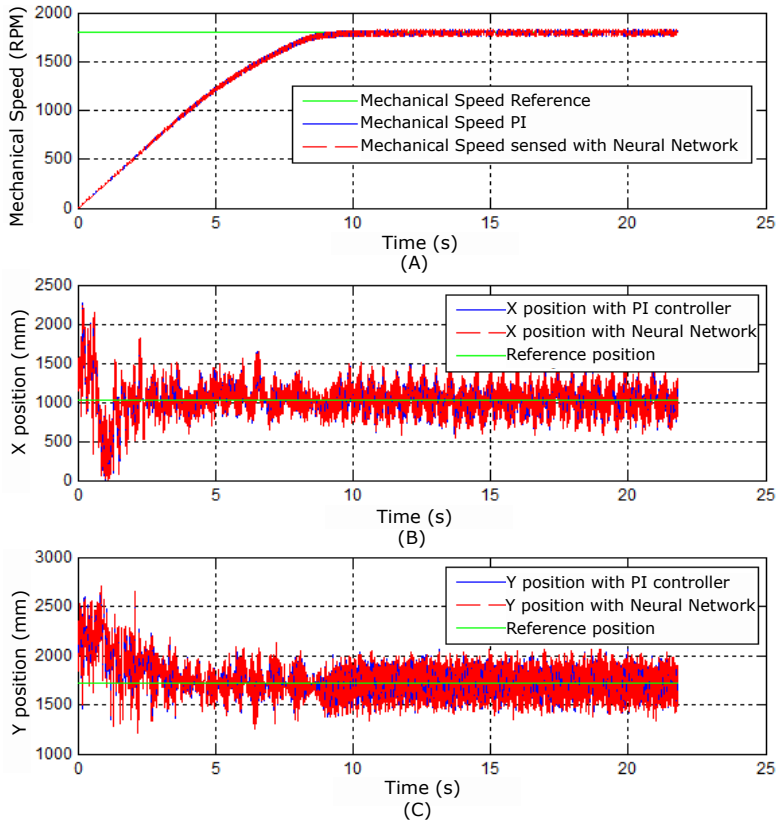


Figure 33. Mechanical speeds and X and Y positions for step speed reference constant.

The legends of the graphs in the experiments present, respectively, the references and the responses with the PI control and with control identified by the colors green, blue, and red. Figure 34 shows the control signal behavior for the implemented controllers.

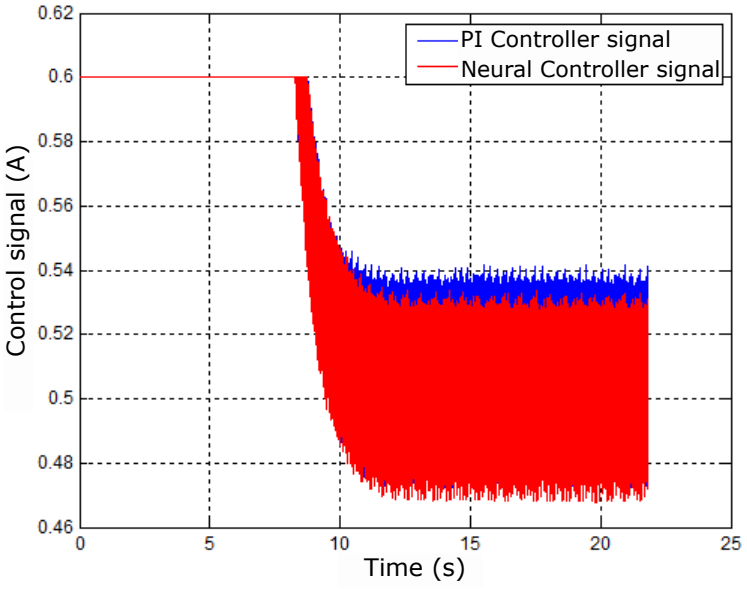


Figure 34. PI and neural control signals for step speed reference.

Figure 34 shows that the control signals are limited due to the motor constraints on the amplitude of 0.6 A, that is, a constraint on the speed control signal for bearing motor operation.

9.3.2. Case Study II—Step Variation

The second experiment presents the system behavior operating at the nominal speed of 1800 rpm with a variation of 5%, that is, operating at 1710 rpm and 1890 rpm. Figure 35 shows the behavior of the mechanical speed and the *X* and *Y* positions referring to the rotor position.

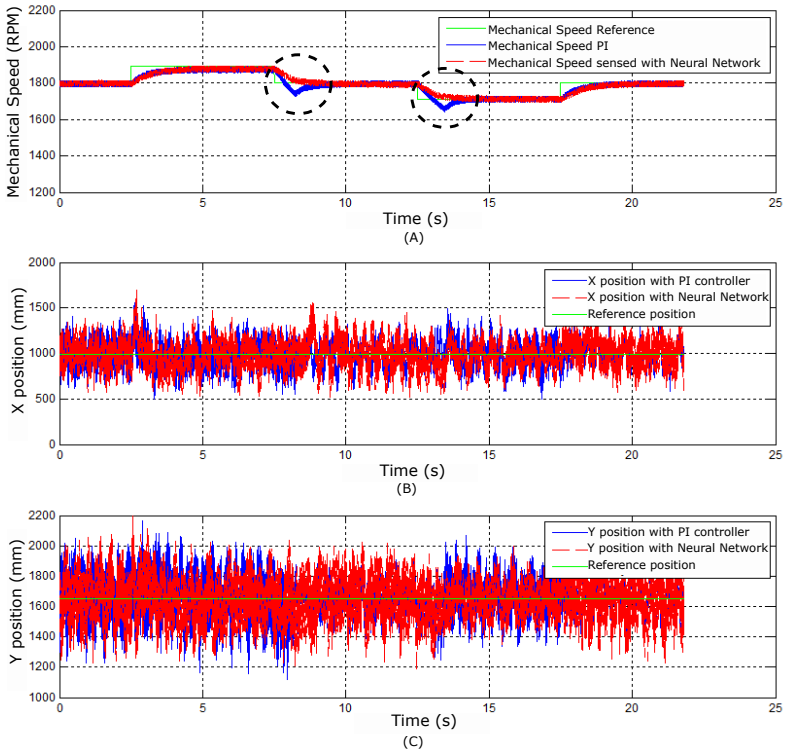


Figure 35. Mechanical speed and *X* and *Y* positions for step speed reference.

In this case, the presence of overshoots in the performance of the The PI controller was identified with dashed circles, which did not occur with the neural controller. This behavior can be seen in Figure 35 because there were higher amplitudes in the PI control signal compared to the neural control. Despite the variations of the control signal in Figure 36, it can be seen that the position control performed well because the *X* and *Y* signs did not suffer variation.

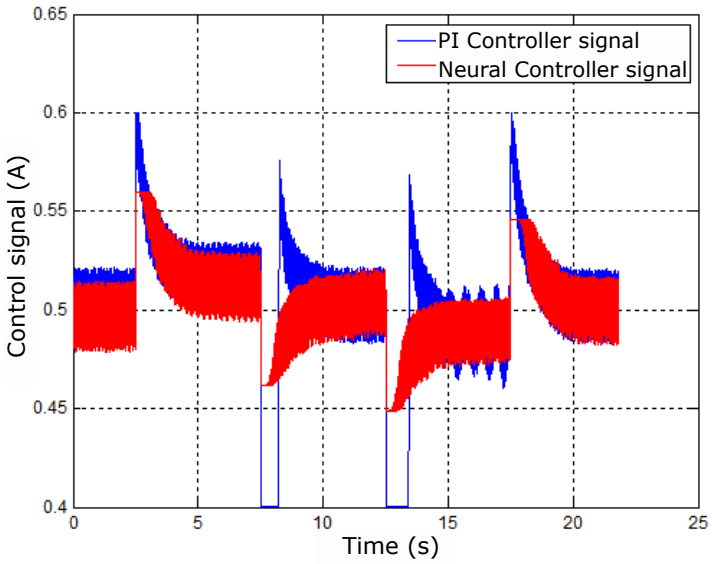


Figure 36. Control signals for step speed reference.

Figure 37 shows the errors of the controllers being acted on by the PI and neural controllers. There is also a difference in amplitude between the controllers due to the effect shown in Figure 35; the responses are also different.

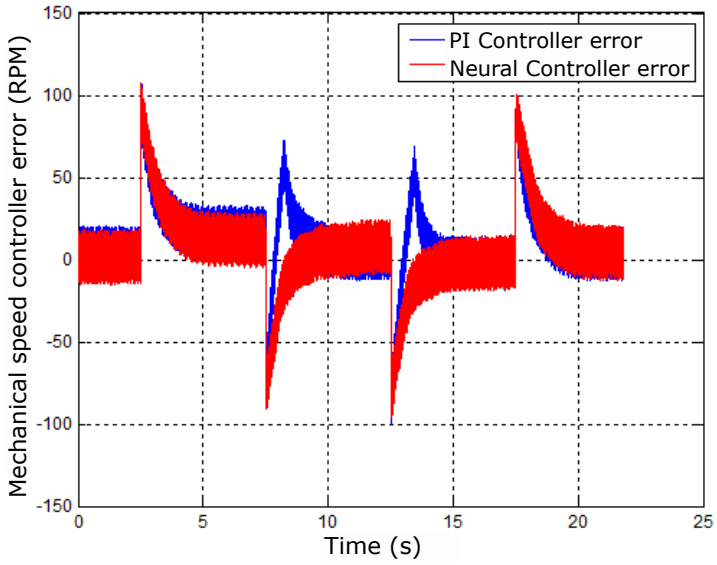


Figure 37. Control error signals for step speed reference.

Thus, even with variations or changes in references in the speed control, Figure 38 shows the dispersion of *XY* signals concentrated, as these variations did not disturb the position control.

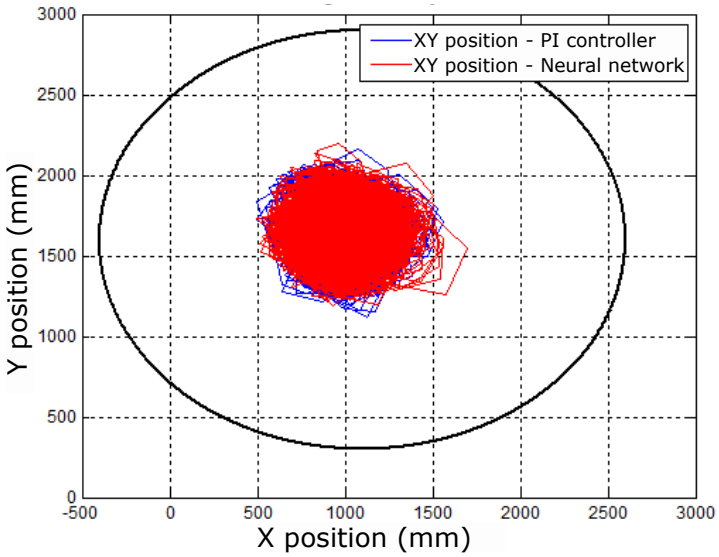


Figure 38. Radial positioning diagrams for step speed reference.

A model DT-2234*B* digital tachometer was used to validate and check the mechanical speed of the rotor operating at 1800 RPM and using the PI and neural controllers. Figure 39 shows the mechanical speed results under regime permanent in Figure 39A working with the PI controller and Figure 39B with the controller neural.



Figure 39. Mechanical velocity measurement (**A**) PI control and (**B**) neural control.

10. Conclusions

The purpose of this article was to present the study and implementation of artificial intelligence techniques for motor-bearing speed control with a split coil. ANFIS Smart Techniques and Neural Networks were investigated and computationally implemented for the evaluation of the motor-bearing performance. The simulated results showed a good performance for the two techniques: as an estimator and as a speed controller, using both an induction motor model operating as a bearing motor. The experimental implementation required adjustments in the interfaces of position, in the speed sensor, and in the replacement of the DSP TMS 3220*F*2812 by the DSP TMS 3220*F*28335, moving from fixed-point floating-point implementation. With the implementation of the motor-bearing system and the analysis of obtained results, some conclusions were possible: the use of DSP 28335 helped in the implementation of the cascade control; the tuning of the current, position, and speed controller, in the experimental results implemented in the DSP *F*28335, was carried out empirically through the trial and error method, whose adjustment is difficult and laborious; current control results were investigated with DC and AC currents, validating the controller tuning in the bearing motor; the position control result has been implemented and tuned to the frequency of 60 Hz, but it presented the best results at the frequencies of 15 Hz, 30 Hz and 45 Hz; the speed control operating conditions were synchronized with the position control, so the motor-bearing system operated properly with current control; the operation of cascaded meshes requires a synchronism between the position control and the speed control because, if it does not occur, the controllers will not achieve stabilization; the speed PI controller had overshoots, and the neural controller system did not present them, demonstrating the ability to learn and generalization of Neural Networks.

Author Contributions: J.R.D.N., J.S.B.L. and A.O.S. conceived and designed the study; J.S.B.L. and D.A.D.M.F., methodology; J.R.D.N. and D.A.D.M.F. performed the simulations and experiments; E.R.L.V., A.R.G.G., J.M.d.S.F. and A.O.S. reviewed the manuscript and provided valuable suggestions; E.R.L.V., J.S.B.L., D.A.D.M.F. and A.R.G.G. wrote the paper; supervision, A.O.S. and J.M.d.S.F. All authors have read and agreed to the published version of the manuscript.

Funding: This research was funded in part by the Coordenação de Aperfeiçoamento de Pessoal de Nível Superior Brasil (CAPES) Finance Code 001 and Conselho Nacional de Desenvolvimento Científico e Tecnológico (CNPq).

Data Availability Statement: The original contributions presented in the study are included in the article, further inquiries can be directed to the corresponding author.

Conflicts of Interest: The authors declare no conflicts of interest.

Abbreviations

The following abbreviations are used in this manuscript:

PWM	Pulse-Width Modulation
DSP	Digital Signal Processor
PI	Proportional Integral
PD	Proportional-Derivative
PID	Proportional Derivative Integral
MSE	Mean Square Error
AEC 5505-04	Sensors
DC	Direct Current

References

1. Victor, V.F.; Quintaes, F.O.; Lopes, J.S.B.; Junior, L.d.S.; Lock, A.S.; Salazar, A.O. Analysis and study of a bearingless AC motor type divided winding, based on a conventional squirrel cage induction motor. *IEEE Trans. Magn.* **2012**, *48*, 3571–3574. [CrossRef]
2. Nunes, E.A.D.F.; Salazar, A.O.; Villarreal, E.R.L.; Souza, F.E.C.; Dos Santos Júnior, L.P.; Lopes, J.S.B.; Luque, J.C.C. Proposal of a fuzzy controller for radial position in a bearingless induction motor. *IEEE Access* **2019**, *7*, 114808–114816. [CrossRef]
3. Carvalho Souza, F.E.; Silva, W.; Ortiz Salazar, A.; Paiva, J.; Moura, D.; Villarreal, E.R.L. A Novel Driving Scheme for Three-Phase Bearingless Induction Machine with Split Winding. *Energies* **2021**, *14*, 4930. [CrossRef]
4. Teixeira, R.d.A.; da Silva, W.L.A.; Amaral, A.E.S.; Rodrigues, W.M.; Salazar, A.O.; Villarreal, E.R.L. Application of Active Disturbance Rejection in a Bearingless Machine with Split-Winding. *Energies* **2023**, *16*, 3100. [CrossRef]
5. Buro, N.G. Magnetic bearings and non-stationary dynamics of rotors. In Proceedings of the Forth International Symposium on Magnectic Bearings, Zurich, Switzerland, 24–26 August 1994.
6. Bu, W.; Li, Z.; Wang, X.; Li, X. A control method of bearingless induction motor based on neural network. In Proceedings of the 2015 IEEE International Conference on Information and Automation, Lijiang, China, 8–10 August 2015; pp. 2252–2257.
7. Depari, A.; Flammini, A.; Marioli, D.; Taroni, A. Application of an ANFIS Algorithm to Sensor Data Processing. *IEEE Trans. Instrum. Meas.* **2007**, *56*, 75–79. [CrossRef]
8. Ding, W.; Liang, D. Modeling of a 6/4 Switched Reluctance Motor Using Adaptive Neural Fuzzy Inference System. *IEEE Trans. Magn.* **2008**, *44*, 1796–1804. [CrossRef]
9. Zhi-xiang, H.; He-qing, L. Nonlinear system identification based on adaptive neural fuzzy inference system. In Proceedings of the International Conference on Communications, Circuits and Systems, Guilin, China, 25–28 June 2006.
10. Vasudevn, M.; Arumugam, R.; Paramasivam, S. Adaptive neuro-fuzzy inference system modeling of an induction motor. In Proceedings of the International Conference on Power Electronics and Drive Systems, 5, Singapore, 19–24 February 2003.
11. Wang, Z.; Liu, X.X. Nonlinear Internal Model Control for Bearingless Induction Motor Based on Neural Network Inversion. *Acta Autom. Sin.* **2013**, *39*, 433–439. [CrossRef]
12. Wang, C.; Zheng, Z.; Guo, D.; Liu, T.; Xie, Y.; Zhang, D. An Experimental Setup to Detect the Crack Fault of Asymmetric Rotors Based on a Deep Learning Method. *Appl. Sci.* **2023**, *13*, 1327. [CrossRef]
13. Ambrożkiewicz, B.; Syta, A.; Georgiadis, A.; Gassner, A.; Litak, G.; Meier, N. Intelligent Diagnostics of Radial Internal Clearance in Ball Bearings with Machine Learning Methods. *Sensors* **2023**, *23*, 5875. [CrossRef] [PubMed]
14. Fu, Z.; Zhou, Z.; Zhu, J.; Yuan, Y. Condition Monitoring Method for the Gearboxes of Offshore Wind Turbines Based on Oil Temperature Prediction. *Energies* **2023**, *16*, 6275. [CrossRef]
15. Yang, Z.; Ding, Q.; Sun, X.; Lu, C. Design and Analysis of a Three-Speed Wound Bearingless Induction Motor. *IEEE Trans. Ind. Electron.* **2022**, *69*, 12529–12539. [CrossRef]
16. Chen, J.; Fujii, Y.; Johnson, M.W.; Farhan, A.; Severson, E.L. Optimal Design of the Bearingless Induction Motor. *IEEE Trans. Ind. Appl.* **2021**, *57*, 1375–1388. [CrossRef]
17. Zhu, H.; Yang, Z.; Sun, X.; Wang, D.; Chen, X. Rotor Vibration Control of a Bearingless Induction Motor Based on Unbalanced Force Feed-Forward Compensation and Current Compensation. *IEEE Access* **2020**, *8*, 12988–12998. [CrossRef]
18. Bian, Y.; Yang, Z.; Sun, X.; Wang, X. Speed Sensorless Control of a Bearingless Induction Motor Based on Modified Robust Kalman Filter. *J. Electr. Eng. Technol.* **2023**, *1*. [CrossRef]

19. Ahn, H.J.; Vo, N.V.; Jin, S. Three-Phase Coil Configurations for the Radial Suspension of a Bearingless Slice Motor. *Int. J. Precis. Eng. Manuf.* **2023**, *24*, 95–102. [CrossRef]
20. Falkowski, K.; Kurnyta-Mazurek, P.; Szolc, T.; Henzel, M. Radial Magnetic Bearings for Rotor-Shaft Support in Electric Jet Engine. *Energies* **2022**, *15*, 3339. [CrossRef]
21. Paiva, J.A. Speed Vector Control of an Induction Machine without Three-Phase Bearings with Split Winding Using Neural Estimation Flux. Ph.D. Thesis, Universidade Federal do Rio Grande do Norte, Natal, Brazil, 2007.
22. *C28x Solar Library: Module User's Guide*; Texas Instruments: Dallas, TX, USA, 2014; v1.2.
23. Gomes, R.R. Bearing Motor with Control Implemented in a DSP. Master's Thesis, UFRJ, Rio de Janeiro, Brazil, 2007.
24. Silva, P.V. Electromagnetic Frequency Regulator Applied in the Wind Generator Speed Control. Ph.D. Thesis, Universidade Federal do Rio Grande do Norte, Natal, Brazil, 2015.
25. Santos, T.H.D. Estimador neural da velocidade do mit acionado por um driver com controle vetorial orientado pelo fluxo do estator. In Proceedings of the XII Simpósio Brasileiro de Automação Inteligente (SBAI), Natal, Brazil, 25–29 October 2015.

Disclaimer/Publisher's Note: The statements, opinions and data contained in all publications are solely those of the individual author(s) and contributor(s) and not of MDPI and/or the editor(s). MDPI and/or the editor(s) disclaim responsibility for any injury to people or property resulting from any ideas, methods, instructions or products referred to in the content.